Rapid high-fidelity multiplexed readout of superconducting qubits

Johannes Heinsoo,[1] Christian Kraglund Andersen,[1] Ants Remm,[1] Sebastian Krinner,[1] Theodore Walter,[1] Yves Salathé,[1] Simone Gasperinetti,[1] Jean-Claude Besse,[1] Anton Potočnik,[1] Christopher Eichler,[1] and Andreas Wallraff[1]

[1]*Department of Physics, ETH Zurich, CH-8093 Zurich, Switzerland*
(Dated: July 11, 2018)

The duration and fidelity of qubit readout is a critical factor for applications in quantum information processing as it limits the fidelity of algorithms which reuse qubits after measurement or apply feedback based on the measurement result. Here we present fast multiplexed readout of five qubits in a single 1.2 GHz wide readout channel. Using a readout pulse length of 80 ns and populating readout resonators for less than 250 ns we find an average correct assignment probability for the five measured qubits to be 97%. The differences between the individual readout errors and those found when measuring the qubits simultaneously are within 1%. We employ individual Purcell filters for each readout resonator to suppress off-resonant driving, which we characterize by the dephasing imposed on unintentionally measured qubits. We expect the here presented readout scheme to become particularly useful for the selective readout of individual qubits in multi-qubit quantum processors.

I. INTRODUCTION

An essential feature of any digital quantum computer or simulator is the ability to measure the state of multiple qubits with high fidelity. In particular, high-fidelity single-shot measurements are needed for determining the result of quantum computation [1], observing error syndromes in quantum error correction [2, 3] and for achieving high channel capacity in quantum communication protocols such as quantum teleportation [4, 5]. Moreover, quantum non-demolition measurements are used for conditioning quantum state initialization [6–8]. Recent progress in scaling up quantum processors based on superconducting qubits has stimulated research towards multiplexed readout architectures with the goal of reducing device complexity and enhancing resource efficiency as discussed in more detail below [9–11].

Superconducting qubits are most commonly measured by employing their off-resonant coupling to a readout resonator [12, 13]. This dispersive interaction results in a qubit-state dependent shift of the resonator frequency, which is probed using coherent microwave fields. Recent improvements in the efficiency of microwave parametric amplifiers [14–17] have enabled single-shot dispersive qubit readout with high fidelity [18, 19]. Furthermore, the use of Purcell filters [11, 20, 21] led to the implementation of faster readout circuits resulting in a reduction of the readout time down to 50 ns for single qubits without introducing additional qubit decay [22].

Extensions of dispersive readout to multiple qubits can be realized by either coupling multiple qubits to a single readout resonator [23, 24] or by probing several readout resonators coupled to a single feedline with a multi-frequency pulse [9]. The latter approach allows for selective readout of any subset of the qubits by choosing the corresponding frequency components in the measurement pulse. High-fidelity frequency multiplexed readout has first been achieved with multiple bifurcation amplifiers [10], one for each qubit, and more recently by employ-

ing a single broadband parametric amplifier [11, 25–27]. Multiplexed readout with Purcell protection has been achieved by coupling multiple readout resonators to a single resonator based Purcell filter [28]. Broadband Purcell filters based on stepped impedance resonators have also been realized [29]. Other recent multi-qubit experiments either employ individual readout lines for each qubit [30, 31] or avoid Purcell decay of qubits by using narrowband readout resonators [28, 29, 32–34], which, however, increase the time required for high-fidelity qubit readout.

In this work, we demonstrate frequency multiplexed readout of up to five qubits using a single readout channel, see Fig. 1 (a) for a schematic of the concept. We use individual Purcell filters for each readout resonator, which in addition to protecting the qubits from Purcell decay, also suppress the off-resonant driving of untargeted readout resonators, thus avoiding the unintentional dephasing of qubits. We characterize this readout crosstalk in our experiments, by analyzing correlations in the readout between all pairs of qubits and by measuring the additional dephasing imposed on untargeted qubits during the readout.

The presented multiplexed readout concept is expected to be particularly useful in multi-qubit algorithms, in which subsets of qubits are measured while other qubits evolve coherently. In the surface code [35], for example, a set of ancillary qubits is repeatedly measured while keeping all data qubits ideally unperturbed. Other examples for protocols relying on readout of individual qubits during the algorithm include the iterative quantum Fourier transform [36], entanglement distillation [37], and deterministic entanglement swapping [38].

II. CONCEPT OF READOUT ARCHITECTURE

For readout we dispersively couple each qubit Qi to a resonator Ri with resonance frequency $\omega_{\mathrm{R}i}$, see Fig. 1 (a). The readout resonator is coupled through a dedicated
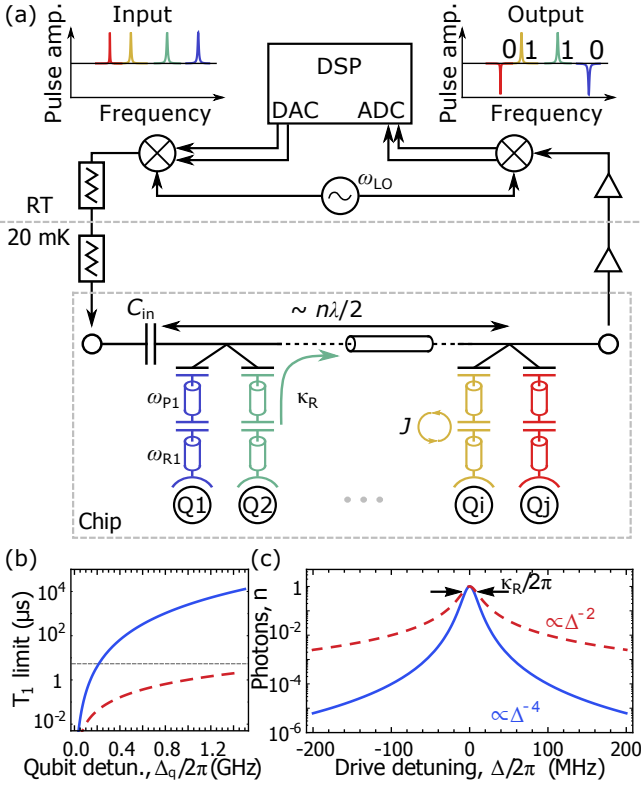
FIG. 1. (a) Schematic of the multiplexed readout experiment showing a circuit diagram of the superconducting chip at $T \approx 20\,\mathrm{mK}$ and the room temperature (RT) electronics. Multi-frequency pulses used for readout are synthesized with a digital signal processing (DSP) unit, then upconverted to microwave frequencies by analog mixing with a local oscillator (LO) field, and applied to the input port of the feedline after several stages of attenuation. The readout signal emitted from the sample is amplified, downconverted and digitized with an analog-to-digital (ADC) converter and further processed with the same DSP unit used for pulse synthesis. (b) Qubit lifetime T_1 as limited by the Purcell effect vs. qubit detuning with (blue solid line) and without (red dashed line) Purcell filter. The dashed line at $T_1 = 5\,\mu\mathrm{s}$ indicates typical T_1 times measured in this work. (c) Calculated photon number in the readout resonator with $\kappa_R/2\pi = 20\,\mathrm{MHz}$ normalized to its maximum value as a function of drive detuning $\Delta = \omega_d - \omega_\mathrm{R}$ with (blue solid line) and without (red dashed line) Purcell filter.

Purcell filter Pi to a common feedline. The effective linewidth of the readout resonator is given by

$$\kappa_\mathrm{R} = \frac{1}{2}\left(\kappa_\mathrm{P} - \mathrm{Re}\left\{\sqrt{-16J^2 + (\kappa_\mathrm{P} - 2i\Delta_\mathrm{R,P})^2}\right\}\right),$$

(1)

with the linewidth of the Purcell filter κ_P, the coupling strength J and detuning between readout resonator and Purcell filter $\Delta_\mathrm{R,P} = \omega_\mathrm{R} - \omega_\mathrm{P}$, see Appendix C for details. In order to achieve fast readout we targeted an effective linewidth of $\kappa_\mathrm{R}/2\pi \gtrsim 10\,\mathrm{MHz}$. Taking a realistic detuning of $\Delta_\mathrm{R,P}/2\pi \times \lesssim 5\,\mathrm{MHz}$ into account, which results from the finite accuracy of circuit design and fabrication, we

design $J/2\pi = 10\,\mathrm{MHz}$ and $\kappa_\mathrm{P}/2\pi = 40\,\mathrm{MHz}$ to approach our targeted κ_R. Furthermore, the Purcell filter parameters are designed to strongly suppress qubit decay into the feedline [20, 39]. As illustrated in Fig. 1 (b), for typical detunings $\Delta_q = \omega_\mathrm{Q} - \omega_\mathrm{R}$ between qubit and resonator the T_1 limit imposed by Purcell decay through the readout resonator is expected to be significantly higher than the typical T_1 times measured in our current device.

For realizing frequency multiplexed readout all Purcell filters are coupled to a common feedline and have an approximately equal frequency spacing of $\Delta_\mathrm{R}/2\pi \approx 160\,\mathrm{MHz}$. Choosing this relatively small frequency spacing in combination with a large κ_R, could induce significant population in untargeted resonators while driving another resonator nearby in frequency. Such unintentional resonator population causes additional dephasing of untargeted qubits [40]. The use of dedicated Purcell filters, however, strongly suppresses the off-resonant driving of each individual readout resonator. In the limit of large drive detuning the intra-resonator photon number scales as $\propto \Delta^{-4}$ with a Purcell filter, as compared to $\propto \Delta^{-2}$ without it, see Fig. 1 (c).

To read out multiple qubits simultaneously we synthesize a multi-frequency probe pulse using a digital signal processing (DSP) unit and then upconvert, attenuate and apply the pulse to the input port of the feedline. A capacitor C_in at the input provides directionality to the readout signal, which preferentially decays from the resonator towards the output port and thus minimizes signal loss into the input port. For the chosen capacitance of $C_\mathrm{in} = 40\,\mathrm{fF}$, a proportion of $(1 + |\Gamma|^2)/2 \approx 98\,\%$ of the readout signal propagates towards the output port, where $\Gamma(\omega) = 1/(1 + 2i\omega Z_0 C_\mathrm{in})$ is the reflection coefficient of the capacitor, see Appendix C for details. Moreover, the capacitor C_in enforces voltage antinodes at positions separated from it by integer multiples of half the wavelength $n\lambda_{\mathrm{R}i}/2$, to which we couple the Purcell filters.

The output signal emitted from the sample is amplified by a traveling wave parametric amplifier (TWPA), a broad-band near-quantum-limited non-degenerate amplifier with an average gain of $20\,\mathrm{dB}$ in the relevant bandwidth 6.5–$7.8\,\mathrm{GHz}$ and a compression point of $P_{1\,\mathrm{dB}} = -100\,\mathrm{dBm}$ [26]. After several additional stages of amplification (see Appendix A) the readout signal is downconverted and digitized with the same DSP unit as used for pulse synthesis. As the DSP unit has a total bandwidth of $1.2\,\mathrm{GHz}$ we can read out the state of up to eight qubits given our choice of detuning Δ_R. The digitized signal is filtered in parallel for each readout frequency with a mode matched filter implemented by weighted integration. The combination of asymmetric feedline, a near quantum limited amplifier, and mode matched filtering results in a total average measurement efficiency of $\eta = 49\,\%$, see Appendix F.
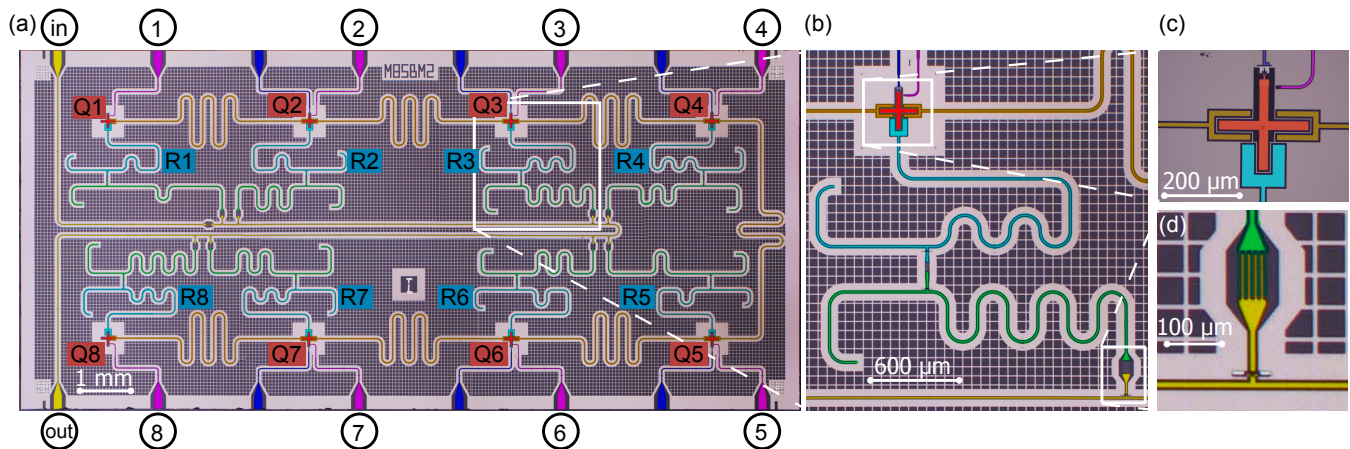
FIG. 2. (a) False-colored optical micrograph of the device with qubits Qi (red), readout resonators Ri (blue), the Purcell filters (green), the coupling bus resonators (orange), the charge lines for single qubit manipulation (purple), the flux lines for single qubit tuning (dark blue) and the feedline (yellow). The ports used for probing the device are denoted in circles. (b) Enlarged view of Q3 with its readout resonator and Purcell filter. (c) Cross-shaped single island qubit capacitavely coupled to a readout resonator, qubit-qubit coupling resonators and a charge line, and inductively coupled to a flux-line. (d) Finger capacitor coupling the Purcell filter to the feedline.

III. DEVICE DESCRIPTION AND CHARACTERIZATION

We demonstrate the concept described above, with a device featuring eight single island transmon qubits [41, 42], see Fig. 2. Each qubit has an individual drive-line to perform single-qubit gates and all but Q1 and Q8 have a flux-line for frequency tuning, as the number of ports on the sample mount is limited. While the readout resonators and Purcell filters are implemented as $\lambda/4$ resonators, qubit-qubit coupling resonators are realized as $\lambda/2$ resonators. The planar Nb and Al structures on the sapphire substrate of the device were defined using photo- and e-beam lithography, for fabrication details see Appendix B.

Transmission spectra measured from the eight qubit drive-lines to the output port reveal a single peak for each readout resonator, see Fig. 3 (a). The frequency spacing between individual resonator frequencies is close to the designed value of 160 MHz. We extract linewidths $\kappa_{\mathrm{R}i}/2\pi$ between 3 MHz and 11 MHz. We attribute additional features in the measured spectra to the residual direct coupling between the drive-lines to other elements on the chip, as well as the finite detuning between the readout resonators and their corresponding Purcell filters.

We measure the state-dependent dispersive shift χ for each qubit by preparing either the ground or excited state before probing the transmission from the input to the output port of the feedline, see Fig. 3 (b) for example data for Q6. We observe a wide dip in the transmission spectrum resulting from the Purcell filter and an additional peak in the center close to the frequency of the readout resonator. The frequency of this peak depends on the qubit state while the background, dominated by the

Purcell filter response, remains largely unaffected. The measured transmission data around a single resonance is well reproduced by the analytic expression obtained from the input–output theory, see Appendix C. From fits of this model to all measured data sets we obtain the resonator parameters summarized in Table I. The effective linewidths and dispersive shifts of most qubits are smaller than the target values discussed in Section II owing to imprecisions in device fabrication. To achieve detunings $\Delta_{\mathrm{R,P}}$ between readout resonator and Purcell filter below 20 MHz across the entire sample we carefully modeled the microwave properties of the individual elements as discussed in Appendix D.

We perform time-resolved measurements of the resonator response to a 80 ns long probe pulse for both the qubit initially prepared in the ground and excited states, see Fig. 4. We show the measured response downconverted to the frequency of the probe pulse and chose the phase such that the real part of the difference between the ground and excited state response is maximal. At the start and the end of the readout pulse we observe a peak and a dip, respectively, which are both independent of the qubit state. We attribute this feature to the fast ring-up and ring-down dynamics of the Purcell filter. In addition, we observe a smooth change in the difference between the ground and excited state responses stemming from the qubit-resonator dynamics. The oscillations in the signals and their difference result from a two-frequency beating caused by the finite quadrature imbalance of the downconversion mixer.

We measured the difference between ground and excited state response of all readout resonators, the complex conjugate of which we use as the integration weights in the DSP unit. Choosing this quantity as a mode matched
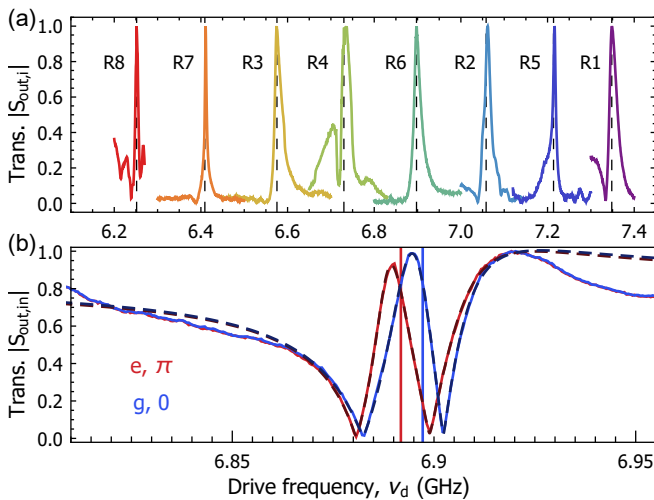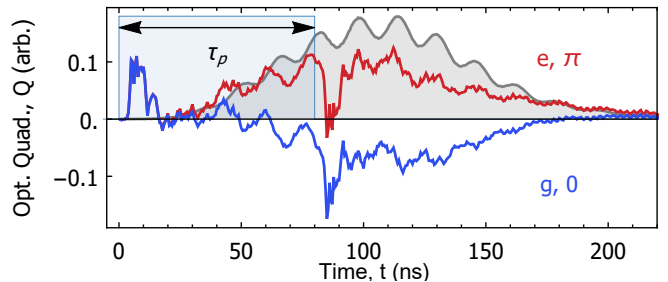
FIG. 4. The complex averaged time dependent response of resonator R6 for Q6 prepared in the exited (red) and ground (blue) state in the quadrature with largest integrated difference. The light blue area indicates the applied readout pulse of length $\tau_p = 80\,$ns and the gray area marks the the difference between the response for the two states.

FIG. 3. (a) Transmission spectra $|S_{\mathrm{out},i}(\nu_d)|$ of the readout resonators measured from the charge line ports i to feedline output port as a function of drive frequency ν_d. (b) Transmission spectrum $|S_{\mathrm{out,in}}(\nu_d)|$ measured from the feedline input to output port close to the resonance frequency of R6 with (red line) and without (blue line) a π-pulse applied to qubit Q6 prior to measurement. The dashed lines are fits to the model described in Appendix C with vertical lines indicating the fitted readout resonator frequencies for the two cases.

filter is known to provide near optimal filter efficiency for a given readout frequency and power [43, 44].

IV. MULTIPLEXED SINGLE-SHOT READOUT

We quantify the performance of single-shot readout for each qubit by preparing the qubit in either the ground or the excited state and by subsequently applying a readout pulse at the corresponding readout resonator frequency. The integrated response signal s for the two input states follows a bimodal Gaussian distribution with the distribution width σ as shown in Fig. 5 for the qubits Q2 and Q6 having the smallest and largest SNR $= (\langle s\rangle_\pi - \langle s\rangle_0)/\sigma$.

	R2	R3	R5	R6	R7
$\omega_R/2\pi$ (GHz)	7.058	6.575	7.214	6.898	6.409
$\omega_P/2\pi$ (GHz)	7.057	6.580	7.196	6.898	6.392
$\kappa_P/2\pi$ (MHz)	32.2	35.6	57.8	38.3	32.6
$J/2\pi$ (MHz)	9.2	7.9	6.9	8.7	7.8
$\kappa_R/2\pi$ (MHz)	14.3	7.8	4.5	11.3	3.1
$\chi/2\pi$ (MHz)	-4.05	-1.11	-4.80	-2.66	-1.92

TABLE I. Parameters of readout resonator Ri obtained from fits to transmission spectra equivalent to the one shown in Fig. 3 (b). The Purcell filter frequency ω_P, readout resonator frequency ω_R, Purcell filter linewidth κ_P and their coupling rate J, the effective readout resonator linewidth κ_R and dispersive shift χ are listed.

We normalize s by the width of the distribution σ to make the SNR easily comparable for the different qubits. Each qubit state is prepared $n_{\mathrm{rep}} \approx 1.3 \times 10^6$ times. In all experiments we also apply an additional readout pulse prior to the state preparation to herald the ground state [6, 7, 22]. The heralding discards $p_{\mathrm{therm}} = 4$–$6\,\%$ of the experiments for each qubit corresponding to the probability for the qubit to be thermally excited [45].

In order to assign a binary value corresponding to the outcome of the qubit measurement from the continuous valued signal s, we choose an assignment threshold, which best separates the prepared states of the qubit. We quantify the fidelity of the readout by the correct assignment probability $P_c = [P(g|0) + P(e|\pi)]/2$, where π (0) marks the state preparation with (without) a π-pulse, and e (g) stands for the qubit assigned as in excited (ground) state. We maximize the assignment probability P_c by optimizing the readout power and frequency for a given readout pulse length for each qubit individually.

The bimodal Gaussian fits to the single-shot histograms provide information on the sources of readout error [22]. There are three main error mechanisms: First, due to finite SNR, the two states cannot be fully distinguished because of the overlap of the two Gaussians. The overlap error accounts for less than 0.5% error probability for qubits Q3, 5, 6&7. For Q2 this error amounts to 3.1% owing to the lower readout power used for this qubit compared to all others. Qubit state mixing between the ground and excited states due to the readout tone [46] causes an error probability $P(e|0) = 0.1$–$1\,\%$. Finally, when prepared in the excited state, the qubit may decay before or during the readout, which accounts for the reminder of the observed errors and ranges from 0.7% for Q3 to 5.5% for Q5 which has a combination of a slow readout resonator and low T_1 compared to the other qubits, see Appendix B for a comparison of parameters. Overall qubit decay appears to be the dominant source of error, which suggests that significant improvements in the readout performance are possible in future devices featuring longer T_1 times.

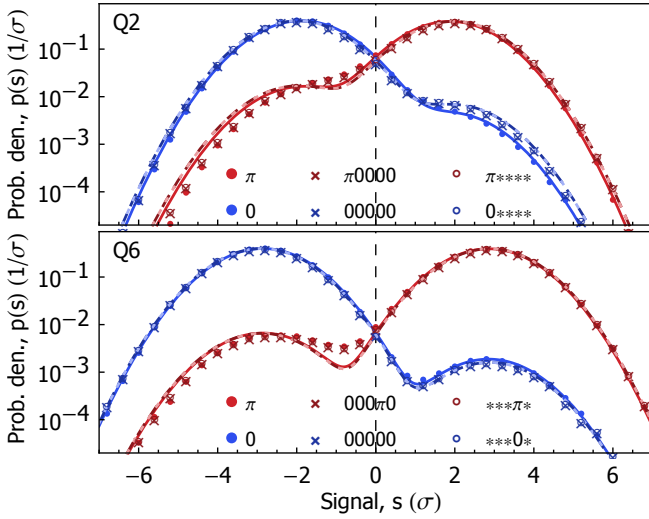We repeat the single-shot readout experiment with

FIG. 5. Histograms of integrated single-shot readout signal of Q2 and Q6 respectively prepared with a π-pulse (red) and without (blue). The signal s is normalized by the width of the gaussian distribution. The experiment data (dots), simultaneous fits to a double Gaussian distribution (solid lines) characterized with their different mean values and equal width. Individual readout, readout pulse applied also to all other qubits in a ground state (darker tones, 0) or averaged over all states of other qubits (brighter tones, $*$).
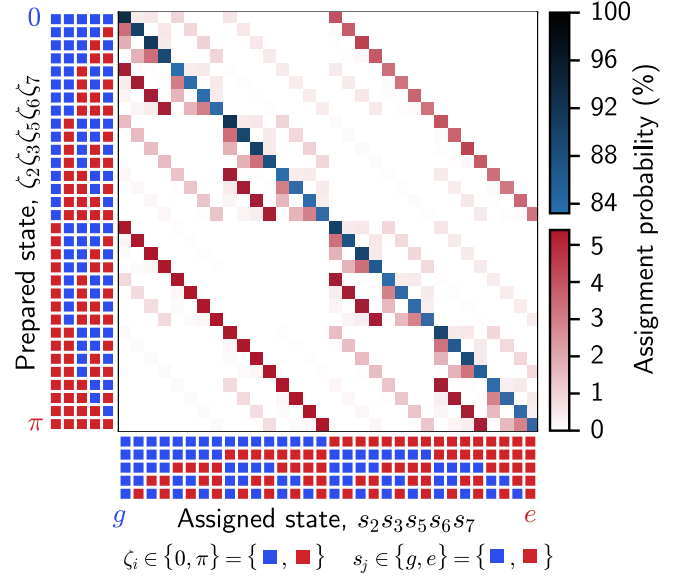

FIG. 6. Assignment probability matrix $P(s|\zeta)$ for each qubit Qi prepared with a π-pulse $\zeta_i = \pi$ (red) or without a pulse $\zeta_i = 0$ (blue) and each qubit assigned to either ground state $s_i = g$ (blue) or exited state $s_i = e$ (red). The qubits are ordered as Q2, Q3, Q5, Q6 and Q7 from left to right (top to bottom) for the prepared (assigned) state.

probe pulses applied at all five readout frequencies simultaneously and with the qubits prepared in all $2^5 = 32$ combinations of basis states. From this dataset we first pick a subset, where all but one qubit are left in the ground state. The histograms with a single (dots) and multi qubit probe tone (crosses) are practically indistinguishable, see Fig. 5. This indicates, that the probe tones do not have a significant spectral overlap with the mode matched filters of the other qubits. Moreover the signal distributions, obtained after averaging over all possible states of the other qubits (circles) are also almost identical. Thus each frequency component contains information about a single qubit only, which is confirmed by the nearly identical correct assignment probability for the individual readout P_{c1} and 5-qubit readout P_{c5} shown in Table II. The remaining discrepancy is on the level of variation of assignment probabilities in repeated experiments.

As the readout performance for each qubit remains largely undisturbed by the additional readout tones we use the individually obtained assignment threshold values

and mode-matched filters. The ability to independently calibrate each subsystem is desired for system scalability.

The probability matrix $P(s_1 \cdots s_5 | \zeta_1 \cdots \zeta_5)$ (Fig. 6) of assigning state $s_i \in \{e, g\}$ for preparation $\zeta_i \in \{0, \pi\}$ describes all state assignment. Ideally, $P(s|\zeta)$ is an identity matrix. The matrix obtained from the experimental data is close to diagonal with the largest deviation corresponding to assigning all qubits to the prepared excited states $P(eeeee|\pi\pi\pi\pi\pi) = 83.3\,\%$ as this input state is most susceptible to individual qubit decay. Apparent features in the full assignment probability matrix are the additional off-diagonal lines, which below the diagonal are indicative of individual qubit decay and above the diagonal of measurement induced excitation during the measurement. These off-diagonal elements are most pronounced for Q2 and Q5, which have the largest decay and mixing errors. Moreover, as discussed in Appendix E, the cross correlations extracted from the assignment probability matrix are up to 0.2%, which is small compared to the single qubit readout errors.

V. EFFECT OF MEASUREMENT CROSSTALK ON UNTARGETED QUBITS

As the readout resonators are coupled to a common feedline and have a finite spectral overlap, the readout tone of qubit Qj also populates the readout resonators of untargeted qubit Qi with a qubit state dependent field amplitude b_s, which causes parasitic mea-

	Q2	Q3	Q5	Q6	Q7
P_{c1}	94.2%	98.8%	93.6%	97.9%	97.8%
P_{c5}	94.5%	98.8%	92.9%	98.6%	97.9%

TABLE II. Correct assignment probability P_{c1} & P_{c5} of the single qubit & simultanious 5 qubit single-shot readout correspondingly.

surement induced dephasing [40]. While the instantaneous measurement-induced dephasing rate $\Gamma(t) = 2\chi\,\mathrm{Im}\big\{(b_g(t)b_e^*(t))\big\}$ changes during the measurement, the error per readout operation corresponds to the integrated effect of the probe pulse. Thus, we quantify the effect of measurement crosstalk on untargeted qubits as the average dephasing rate $\bar{\Gamma}_{ij} = 1/\tau_p \int_0^\infty \Gamma_{ij}(t)\,dt$ of Qi due to the measurement of Qj with a pulse length τ_p.

We measure the average dephasing rate in a Ramsey experiment [44, 47] with the pulse scheme shown in the inset of Fig. 7 (a). By varying the phase ϕ of the second $\pi/2$-pulse on Qi we observe Ramsey oscillations with a contrast c. In between the $\pi/2$-pulses we apply a probe pulse scaled in amplitude by a factor ξ relative to the final probe pulse. As shown for the example data in Fig. 7 (a) for $i = 7$ and $j = 3$, the Ramsey contrast c decreases with increasing ξ. We fit the observed data to the expression $c(\xi) = c_0 e^{-\bar{\Gamma}\tau_p\xi^2}$ to extract the measurement induced dephasing rate $\bar{\Gamma}$. Here, the constant prefactor c_0 accounts for all other dephasing mechanisms which are independent of ξ.

When we apply the measurement pulse to the same qubit as the Ramsey experiment ($i = j$) we observe the intended measurement induced dephasing. As discussed in Appendix F, the measured $\bar{\Gamma}_{ii}$ in combination with the SNR obtained from the histograms in Fig. 5 allows us to estimate the measurement efficiency η [44], which we find to be 42–52 %, mostly limited by the dissipative components before the TWPA and the internal loss of the TWPA.

The parasitic measurement induced dephasing $\bar{\Gamma}_{ij}$ ($i \neq j$) spans two orders of magnitude (Fig. 7). For example the large dephasing of Q2 when measuring Q5 leads to a phase-error probability due to measurement-induced dephasing of $P_\phi = [1 - \exp(-\bar{\Gamma}_{ij}\tau_p)]/2 \approx 11\%$ while for other qubit pairs the corresponding phase-error probability is below 0.1 %.

To calculate the expected dephasing rate for the sample parameters given in Appendix B, we solve for the field amplitude $b(t)$ in the readout resonator described by the equations of motion given in Appendix C. The comparison of the calculated, depicted with black frame in Fig. 7, and the measured dephasing, depicted with filled bars, shows a qualitative agreement except for the dephasing of Q5, for which we did not obtain reliable data due to qubit frequency instability and short dephasing time, see also Appendix B.

The good agreement with the model of parasitic measurement-induced dephasing justifies using the model for explaining the qualitative features and predicting possible future improvements. For example Q2 is most strongly dephased by the measurement tones in R5 and R6 as these are the readout resonators closest in frequency to R2. The readout pulse for R5 dephases Q2 more strongly compared to the pulse for R6, since a much stronger tone was used for R5 due to its small dispersive shift χ_5. In addition, Q2 shows the largest measurement-induced dephasing in general, as it has the largest χ and one of the largest κ_R
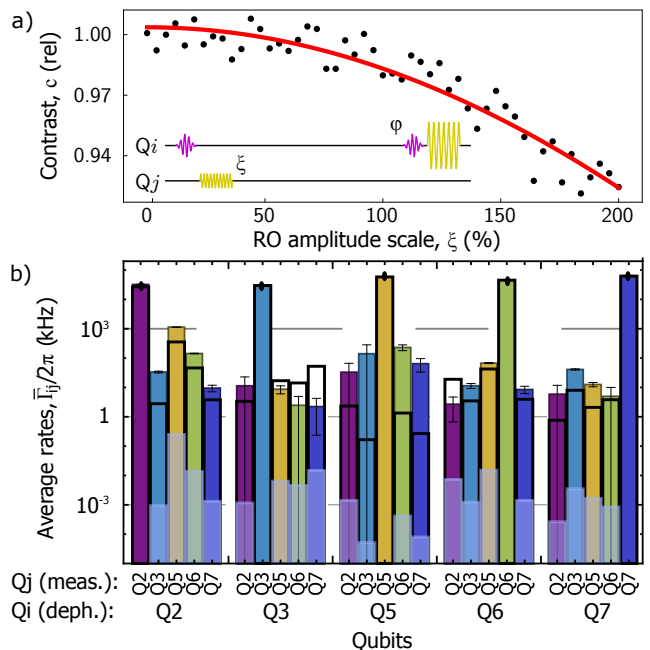

FIG. 7. (a) Contrast of the Ramsey oscillations c of qubit Q7 as for different readout pulse amplitudes ξ on Q3 (dots) and a Gaussian fit (red line). (a inset) Pulse scheme used for the dephasing measurement consisting of 10 ns π-pulses (pink) and 80 ns readout pulses (yellow). (b) The average dephasing rate of qubit Qi when applying a readout pulse to qubit Qj. Experimentally measured rates (filled bars), calculated values based on the parameters extracted from spectroscopy shown in Table I (thick black frames) and calculated dephasing rates for a Gaussian filtered probe pulse (transparent blue bars).

which leads to the largest spectral overlap with the probe pulses targeted to other readout resonators.

As the spectral overlap between the readout resonators is already small, the readout crosstalk is limited by the spectral width of the square shaped probe pulses, which are significantly wider in spectrum than the readout resonators. As shown in light blue in Fig. 7, by convolving the pulse shape with a Gaussian kernel with a width $\sigma = 5$ ns the parasitic measurement-induced dephasing could possibly decrease by 2–3 orders of magnitude. For the same κ_R/Δ_R ratio, but without individual Purcell filters such probe-pulse shaping results in only a minor improvement.

VI. DISCUSSION AND OUTLOOK

In this work we demonstrate frequency multiplexed readout of 5 qubits with high qubit selectivity. We show that the presented architecture enables fast readout in combination with low crosstalk. In particular, we show that the single qubit readout performance remains unaffected by the presence of multiple readout tones at a level where the individual readout calibration can be used for

multi-qubit readout without degrading performance.

The primary source of errors in the single-shot qubit readout are single qubit decay and measurement-induced mixing. Furthermore, we found that the main source of readout crosstalk arose from the probe pulses spanning to the resonance of untargeted readout resonators. From simulations we expect that a significant reduction of parasitic resonator population could be achieved by a Gaussian filtering of the pulses.

Due to the short readout resonator occupation time of 250 ns and potentially low crosstalk, the readout architecture presented in this work seems particularly interesting for quantum error correction algorithms, in which a set of ancilla qubits is repeatedly measured while preserving the coherence of data qubits on the same chip [48].

ACKNOWLEDGMENTS

Appendix A: Experimental setup

A multiplexed readout experiment requires instruments for generating probe pulses, detecting response signal and for manipulating the qubit states. The components for control are operated at different temperature stages of a cryogenic setup as shown in Fig. 8.

The readout pulses are generated and detected at 1.8 GSPS using a single ultra-high frequency lock-in amplifier (*Zurich Instruments* UHFLI). Upon receiving the readout trigger, the virtual AWG component of the built-in FPGA outputs a probe-pulse modulation waveform on the output channel pair. The two channels drive an IQ-mixer on an upconversion board, used for single-sideband upconversion to the radio frequency (RF). Along the way to the superconducting device, the probe pulses are attenuated by 20 dB at the temperatures of 4 K, 100 mK and 12 mK in an ^{3}He–^{4}He dilution cryostat.

After the interaction with the readout resonators, the weak measurement signal is amplified using a wide bandwidth traveling waveguide parametric amplifier (TWPA) [26] with the average gain of $G_{\mathrm{TWPA}} = 20\,\mathrm{dB}$ and a 1dB-compression point of $P_{1\,\mathrm{dB}} = -100\,\mathrm{dBm}$. In order to impedance match the TWPA with its environment, the TWPA is surrounded with a wide-bandwidth isolator on both sides. The pump tone for the TWPA is generated at room-temperature and is added to the signal using a directional coupler at the TWPA input. Before the response pulse arrives at the room-temperature electronics it is bandpass-filtered at the base temperature and further amplified with a high-electron-mobility transistor (HEMT) amplifier at the 4 K stage.

At room temperature the response pulse is amplified with an ultra low noise (ULN) and a low noise (LN) amplifier. The RF amplification is followed by downconversion to an intermediate frequency (IF) and the IF signal is subsequently further amplified. The warm amplification (WAMP) and downconversion (DC) boards feature additional filters and attenuation to suppress out-of-band noise and standing waves. A single local oscillator (LO) is shared by the measurement tone up- and downconversion.

The response signal is digitized by the UHFLI and passed through different digital signal processing components in the FPGA. The first FPGA component averages the incoming timetraces over all trigger events and is used for the data shown in Fig. 4. The single-shot measurement results are collected using parallel weighted integration and logging units. The on-board real-time data analysis gives a significant reduction of data and reduces the time used for uploading and analyzing the high-bandwidth data on a PC.

Each qubit is capacitively coupled to a drive line and inductively to a flux line. The drive pulses are generated using a channel pair of an AWG at 1.2 GSPS. The single-sideband upconversion board has a built-in switch which allows bypassing the mixer without recabling for spectroscopy measurements. The qubit drive lines have the same cold attenuation configuration as the probe tone input. For parking the qubits in the frequency space, a voltage bias is directly applied to the flux-lines. At the 100 mK and 12 mK temperature stages the flux lines are not attenuated, but low-pass filtered with a cutoff at 1 GHz. In addition, the flux lines have EccoSorb filters at the base temperature to suppress high frequency signals left unattenuated by the conventional lowpass filters.

Appendix B: Detailed sample description

In Table III we list a detailed overview of the qubit parameters used in this work. Qubit Q5 exhibited from significant frequency instability and thus appeared at different configurations for the measurement discussed in Section V shown in parenthesis in Table III. The maximum qubit frequency $\nu_{\mathrm{Q,max}}$ is extracted from a two-parameter sweep of the voltage bias and the readout drive frequency
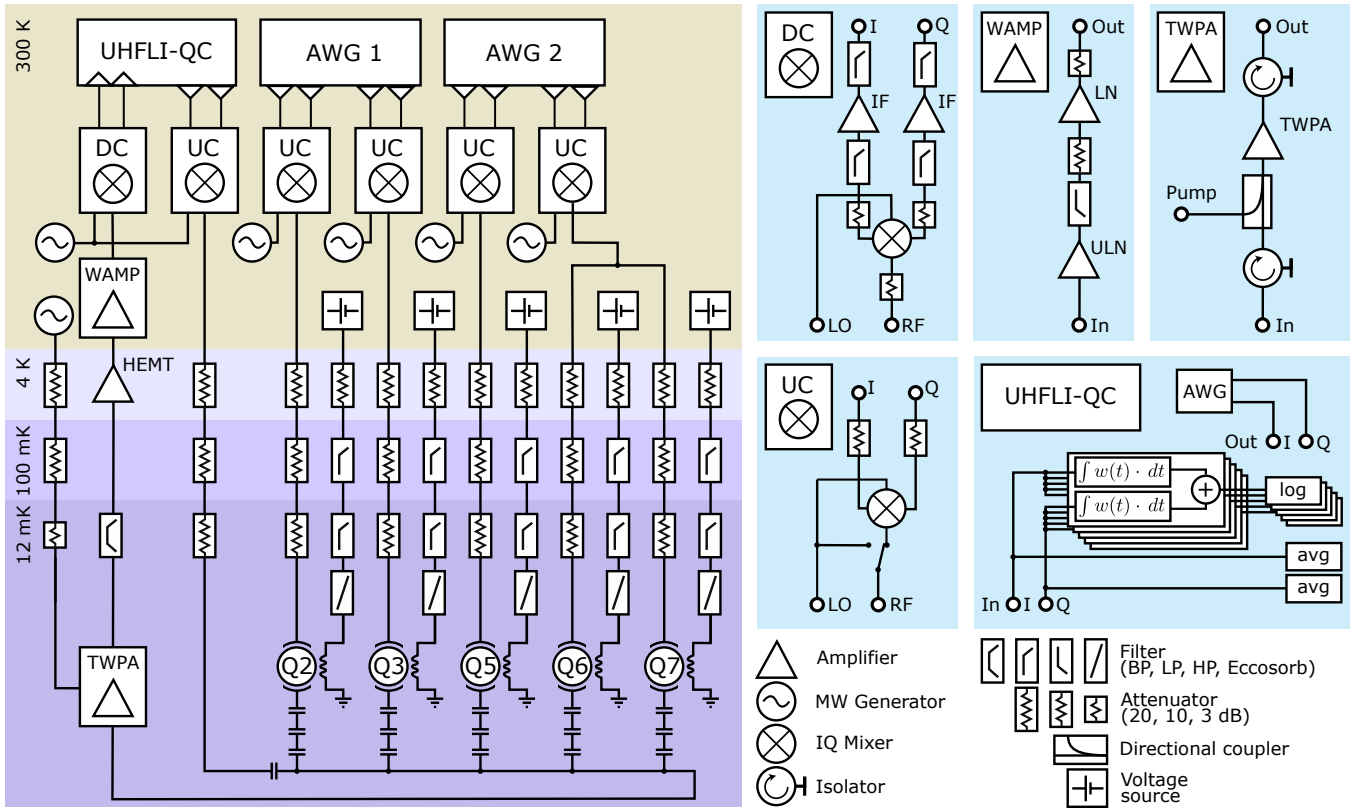
FIG. 8. Description of the electrical setup of the experiment. The colored background on the left side indicates the different temperature stages for the components. In the panels on the right we describe in more detail downconversion (DC), upconversion (UP), warm amplification (WAMP) boards, components used around traveling waveguide parametric amplifier (TWPA) and virtual hardware components of the Zurich Instruments UHFLI-QC. UHFLI-QC includes an internal arbitrary waveform generator (AWG), logging units (log), timetrace averager (AVG) and complex weighted integration units. Amplification chain includes a high electron mobility transitor (HEMT), intermediate frequency (IF), low noise (LN) and ultra low noise (ULN) amplifiers.

to find the sweetspot of the qubit followed by a Ramsey experiment to extract the precise qubit frequency. The anharmonicity of each qubit is extracted by observing two-photon transitions in high-power spectroscopy. The qubit energy relaxation time T_1 and Ramsey decoherence time T_2^* are characterized by standard timedomain experiments. The thermal population of the excited state $P_{\text{therm.}}$ is the probability that the qubit was found to be in the excited state in the preselection readout conducted before every single shot experiment run. For all qubits we used a π-pulse length of 50 ns.

The parameters related to the readout resonators and Purcell filters are obtained as explained in the main text. The frequencies $\nu_{\text{RO mod.}}$ are the intermediate frequencies of the probe pulse and and $\omega_{\text{RO}}/2\pi$ are the corresponding frequencies of the upconverted pulse. The photon number during the readout, n_{RO}, is measured using an AC-stark shift measurement and the critical photon number $n_{crit} = g^2/[4(\omega_Q - \omega_R)^2]$ is calculated from parameters above.

The device was fabricated on a substrate of c-plane cut single side polished sapphire from Rubicon Tech-

nology. A 150 nm thin niobium film was deposited by StarCryoelectronics on wafers cleaned in ultrasound by 50 C acetone and IPA. The rest of the circuit, except the Josephson junctions, is defined by optical lithography and dry etching process. Josephson junctions are formed by Al/AlOx/Al deposited in an electron-beam Plassys evaporator with a Dolan bridge shadow evaporation technique. Native Nb oxide was removed using ion milling before and after defining the e-beam mask.

Appendix C: Input–output theory

As discussed in the main text, the input port of the sample is interrupted by a capacitor in order to improve the efficiency of the qubit state measurement. This impedance mismatch in the feedline, however, changes the density of states in the feedline and therefore the effective linewidth of both the readout resonators and the Purcell filters. In order to understand and predict both the transmission spectrum and readout resonator time dynamics we

	Q2	Q3	Q5	Q6	Q7
Qubit frequency, $\omega_Q/2\pi$ (GHz)	6.254	5.206	6.441 (5.457)	5.902	5.442
Max. qubit frequency, $\omega_{Q,max}/2\pi$ (GHz)	6.260	5.216	6.996	5.996	5.442
Qubit anharmonicity, $\alpha/2\pi$ (MHz)	-226	-246	-198	-234	-238
Qubit lifetime, T_1 (µs)	5.7	6.0	4.9	5.8	5.8
Qubit coherence time, T_2^* (µs)	4.1	2.5	0.7	3.1	7.8
Thermal population, p_{therm}(%)	4.7	5.1	2.9	6.0	6.4
Readout resonator frequency, $\omega_R/2\pi$ (GHz)	7.058	6.575	7.214 (7.200)	6.898	6.409
Purcell filter frequency, $\omega_P/2\pi$ (GHz)	7.057	6.580	7.196	6.898	6.392
Purcell filter linewidth, $\kappa_P/2\pi$ (MHz)	32.2	35.6	57.8	38.3	32.6
Readout-Purcell coupling, $J/2\pi$ (MHz)	9.2	7.9	6.9	8.7	7.8
Effective readout linewidth, $\kappa_R/2\pi$ (MHz)	14.3	7.8	4.5 (11.8)	11.3	3.1
Qubit-coupling to Ri, $g/2\pi$ (MHz)	122.3	123.4	134.0	115.9	108.2
Dispersive shift, $\chi/2\pi$ (MHz)	-4.1	-1.7	-4.8 (-0.9)	-2.6	-2.4
Readout frequency, $\omega_{RO}/2\pi$ (GHz)	7.056	6.572	7.208	6.891	6.407
Readout IF, $\nu_{\text{RO mod.}}$ (MHz)	195	-289	347	30	-454
Readout photons, n_{RO}	4.1	22.2	2.9 (126)	5.8	9.7
Critical photons, n_{crit}	10.8	30.2	8.2 (42)	18.2	19.9

TABLE III. Overview of qubit and resonator properties, see Appendix B for details. The numbers in parentheses for Q5 are the settings used for the dephasing measurements in Sec. V.

construct here an input–output model of two coupled cavities a and b representing the Purcell filter and readout resonator respectively [49].

The equation of motion for this two-mode system is given as

$$\frac{da}{dt} = -i\Delta_a a - \frac{\kappa_a + \gamma_a}{2}a - iJb + \sqrt{\kappa_a}a_i, \quad \text{(C1a)}$$

$$\frac{db}{dt} = -i\Delta_b b - \frac{\kappa_b + \gamma_b}{2}b - iJa + \sqrt{\kappa_b}b_i \quad \text{(C1b)}$$

where $\Delta_{\{a,b\}} = \omega_{\{a,b\}} - \omega_d$ is the detuning between the drive frequency of the input field ω_d and the bare resonance frequency $\omega_{a,b}$ of the respective mode. The rates γ_a and γ_b are the internal loss rates of the resonators. The corresponding input–output relations are

$$a_o = a_i - \sqrt{\kappa_a}a, \quad \text{(C2a)}$$

$$b_o = b_i - \sqrt{\kappa_b}b, \quad \text{(C2b)}$$

where κ_a is the large coupling of the Purcell filter to the feedline and κ_b is the weak coupling of the readout resonator to the qubit drive-line.

A t-junction, such as the connection of the Purcell filter to the feedline, has three ports connected to the Purcell filter mode a, a port on the right r and a port on the left l. For a symmetric, energy conserving and reciprocal 3-port device the relations between the incoming (a_i, l_i and r_i) and outgoing (a_o, l_o and r_o) mode-amplitudes are

$$l_o = -\frac{1}{3}l_i + \frac{2}{3}r_i + \frac{2}{3}a_o, \quad \text{(C3)}$$

$$r_o = \frac{2}{3}l_i - \frac{1}{3}r_i + \frac{2}{3}a_o, \quad \text{(C4)}$$

$$a_i = \frac{2}{3}l_i + \frac{2}{3}r_i - \frac{1}{3}a_o \quad \text{(C5)}$$

where we labeled the incoming and outgoing modes with respect to the Purcell filter. At the input capacitor, a mode c is connected with the port l of the t-junction. The input–output relations of the capacitor in series are:

$$c_o = (1-\Gamma)l_o + \Gamma c_i \quad \text{(C6a)}$$

$$l_i = (1-\Gamma)c_i + \Gamma l_o, \quad \text{(C6b)}$$

where $\Gamma(\omega) = 1/(1 + 2i\omega Z_0 C_{in})$ with the frequency ω, the characteristic impedance Z_0 and the input capacitor capacitance C_{in}.

Combining all the input–output relations and assuming a neglectable dispersion between the t-junction and the capacitor, we eliminate the modes l and a such that the equations of motion becomes

$$\frac{da}{dt} = -i\tilde{\Delta}_a a - \frac{\tilde{\kappa}_a + \gamma_a}{2}a - iJb + \frac{\sqrt{\kappa_a}}{2}\left(\tilde{c}_i + \tilde{r}_i\right), \quad \text{(C7a)}$$

$$\frac{db}{dt} = -i\Delta_b b - \frac{\kappa_b + \gamma_b}{2}b - iJa + \sqrt{\kappa_b}b_i \quad \text{(C7b)}$$

where Γ alters the detuning from the cavity resonance $\tilde{\Delta}_a = \tilde{\omega}_a - \omega_d$, the coupling to the capacitor side input of the transmission line $\tilde{c}_i = (1-\Gamma)c$ and the coupling to the galvanically coupled port of the feedline $\tilde{r}_i = (1+\Gamma)r$. The linewidth, taking into account the altered environment, is

$$\tilde{\kappa}_a = \kappa_a \frac{1 + \text{Re}\{\Gamma\}}{2} \quad \text{(C8)}$$

and similarly the resonator frequency $\tilde{\omega}$ becomes

$$\tilde{\omega}_a = \omega_a + \kappa \frac{\text{Im}\{\Gamma\}}{4} \quad \text{(C9)}$$

where κ_a and ω_a correspond to cavity linewidth and frequency in the limit $\Gamma \to 1$ and the Purcell filter sees a

single port. The input–output relations corresponding to the equations of motion above now read

$$c_o = c_i + (1 - \Gamma)r_i - \frac{\sqrt{\kappa_a}}{2}(1 - \Gamma)a, \qquad \text{(C10a)}$$

$$r_o = r_i + (1 - \Gamma)c_i - \frac{\sqrt{\kappa_a}}{2}(1 + \Gamma)a, \qquad \text{(C10b)}$$

$$b_o = b_i - \sqrt{\kappa_b}b. \qquad \text{(C10c)}$$

To extract the scattering parameters of the system, we solve Eq. C7 for the steady state and substitute the solution into Eq. C10. By setting $r_i = b_i = 0$ this approach yields the transmission coefficient through the feedline

$$\frac{S_{21}}{1 - \Gamma} = \frac{r_o/c_i}{1 - \Gamma} = 1 - \frac{1 + \Gamma}{1 + \text{Re}\{\Gamma\}}$$
$$\times \frac{\tilde{\kappa}_a \left(\gamma_b + 2i\Delta_b + \kappa_b\right)}{4J^2 + \left(\gamma_a + 2i\tilde{\Delta}_a + \tilde{\kappa}_a\right)\left(\gamma_b + 2i\Delta_b + \kappa_b\right)}, \quad \text{(C11)}$$

normalized by the insertion loss induced by the input coupler of the feedline. Equation (C11) is the model fitted to the data in Fig. 3 (b). To obtain the transmission coefficient from the weekly coupled qubit drive line to the output port of the transmission line we set $r_i = c_i = 0$:

$$S_{23} = \frac{r_o}{b_i} = \frac{1 + \Gamma}{\sqrt{2\left(1 + \text{Re}\{\Gamma\}\right)}}$$
$$\times \frac{4iJ\sqrt{\kappa_a}\sqrt{\kappa_b}}{4J^2 + \left(\gamma_a + 2i\tilde{\Delta}_a + \tilde{\kappa}_a\right)\left(\gamma_b + 2i\Delta_b + \kappa_b\right)} \quad \text{(C12)}$$

which describes the data shown in Fig. 3 (a).

The inverse linewidth of readout resonator sets, as discussed in the main text, a limit to the readout time. When the Purcell filter decay rate κ_a is significantly larger than the coupling rate J, the effective linewidth of the readout resonator becomes [39]

$$\kappa_{\text{R}} = \frac{4J^2\tilde{\kappa}_a}{\tilde{\kappa}_a^2 + 4\tilde{\Delta}_{\text{ab}}^2}, \qquad \text{(C13)}$$

here neglecting all effects of $\gamma_{a,b}$ and κ_b as these are typically small. However, we need to place N readout structures into the finite detection bandwidth Δ_D. Therefore, to avoid crosstalk from spectral overlap of the readout resonators, we have a practical limit to resonator linewidth $\kappa_a \lesssim \Delta_D/(nN)$, where $n \sim 4$ is the amount of linewidths between each resonator frequency. Thus the assumption $\kappa_a \gg J$ may break down. To extract the exact expression for κ_{R} Eq. C7 is diagonalized and the real part of the eigenvalue corresponding to the readout resonator mode is the effective linewidth. Thus, we obtain

$$\kappa_{\text{R}} = \frac{1}{2}\left(\tilde{\kappa}_a - \text{Re}\left\{\sqrt{-16J^2 + \left(\tilde{\kappa}_a - 2i\tilde{\Delta}_{\text{ab}}\right)^2}\right\}\right), \qquad \text{(C14)}$$

which is the expression used to calculate the readout resonator linewidth in Table I from the fitted parameters. In the main text we denote the Purcell resonator frequency $\tilde{\omega}_a = \omega_{\text{P}}$ and the linewidth $\tilde{\kappa}_a = \kappa_{\text{P}}$.

Appendix D: Calculating the resonator frequencies

Both the Purcell filter and the readout resonator for each qubit are realized as $\lambda/4$-resonators on the device used in this work. The open ends of the $\lambda/4$-resonators are capacitively coupled to either a qubit or to the feedline, see Fig. 2 (c) and (d). Moreover, each pair of Purcell filter and readout resonator are coupled together with a capacitor, C_c, at a position x_c from the terminated end of the resonators. The field amplitude between the terminated end and the coupling point $x = x_c$ and between the coupling point and the open end is described by the standard wave equation. Thus, the mode function for the phase variable $\phi(x,t)$ (time-integral of the voltage) of each resonator is given as [50]

$$\phi(x,t) = \phi_0(t) \times \begin{cases} B\sin(kx) & \text{for } 0 \leq x \leq x_c \\ \cos[k(x - d) - \theta] & \text{for } x_c \leq x \leq d, \end{cases} \quad \text{(D1)}$$

where ϕ_0 is the time dependent field amplitude, d is the length of the resonator, B is a unitless scaling factor set by the boundary condition, θ is a phase offset, $k = \omega/v$ is the wave number and ω is the resonance frequency of the mode. Moreover, $v = 1/\sqrt{lc}$ is the phase velocity of field with l and c as the inductance and capacitance per length of the resonator respectively. This choice of mode function explicitly sets the boundary condition at $x = 0$ where the resonator is grounded, while the phase θ is set by the boundary condition at the position d. As shown in [50], the Euler-Lagrange equation at d gives the equations of motion

$$\ddot{\phi}(d,t) + \frac{1}{C_0l}\frac{\partial}{\partial x}\phi(x,t)\bigg|_{x=d} = 0, \qquad \text{(D2)}$$

where C_0 is the sum of capacitance to ground and to the qubit (feedline) for the readout resonators (Purcell filters). From the wave equation it follows that $\ddot{\phi}(x,t) = -\omega^2\phi(x,t)$, such that Eq. (D2) can be re-written into

$$\tan(\theta) = C_0Z_0\omega \qquad \text{(D3)}$$

where $Z_0 = \sqrt{l/c}$ is the characteristic impedance of the co-planar waveguide. The final boundary condition to consider is at the coupling capacitor at $x = x_c$. Since the mode has to be continuous the scaling factor becomes

$$B = \frac{\cos[k(x_c - d) - \theta]}{\sin(kx_c)}. \qquad \text{(D4)}$$

As the sum of the currents at x_c has to be zero, we get the corresponding equation of motion [50]

$$\ddot{\phi}(x_c,t) + \frac{1}{C_c l}\left(\left.\frac{\partial}{\partial x}\phi(x,t)\right|_{x=x_{c+}} - \left.\frac{\partial}{\partial x}\phi(x,t)\right|_{x=x_{c-}}\right) = 0 \tag{D5}$$

where C_c is the coupling capacitance. As above this equation reduces to

$$\tan(kx_c)^{-1} + \tan[k(x_c - d) - \theta] = C_c Z_0 \omega. \tag{D6}$$

Now we can solve Eqs. (D3) and (D6) numerically to find ω and θ for a given resonator length and with the capacitances C_0 and C_c obtained from finite element simulations. Using these solutions we can accurately predict the frequency of each resonator, which ensures that the readout resonators are on resonance with its Purcell filters and that we achieve equidistant spacing of the resonators of the different qubits.

Appendix E: Correlations and cross assignment fidelity output

There are in general many ways of quantifying crosstalk in the state assignment for different qubits and here we will discuss cross fidelity and cross correlations.

In the main text we present the probabilities for assigning each multi-qubit state to the prepared state, which we denote $P(s|\zeta)$ with s referring to the assigned state and ζ to the prepared state. From the marginal distributions, we can now quantify the information of qubit Qj in the assignment of qubit Qi by the cross-fidelity:

$$F_{ij} = \langle 1 - P(e_i|0_j) - P(g_i|\pi_j)\rangle, \tag{E1}$$

where e_i (g_i) denotes the assignment of Qj to the excited (ground) state, π_j (0_j) denotes the preparation with (without) a π-pulse on Qi and the average $\langle \cdot \rangle$ is taken over assignment (preparation) of all qubits but i (j). We have extracted F_{ij} from the experimental data presented in presented Fig. 6 and as shown in Fig. 9 the off-diagonal elements are small. Ideally, the outcome of Qi should be uncorrelated with Qj so we expect $P(e_i|0_j) = P(g_i|\pi_j) = 0.5$ and the off-diagonal elements should be 0. However, the correlations remain significantly below the individual readout infidelities obtained from the diagonal of F_{ij} and thus we expect each weighted measurement band give information only about a single qubit. This is also in agreement with mode-matched filter having a very small spectral overlap. Single qubit errors therefore appears to dominate the imperfections of the qubit assignment.

The cross-fidelity F_{ij} has a functional importance, as it shows if the state assignment of a qubit is affected by prepared the state of the others. However, as the readout threshold and mode-matched filter are optimized for the assignment of each qubit, a readout tone applied
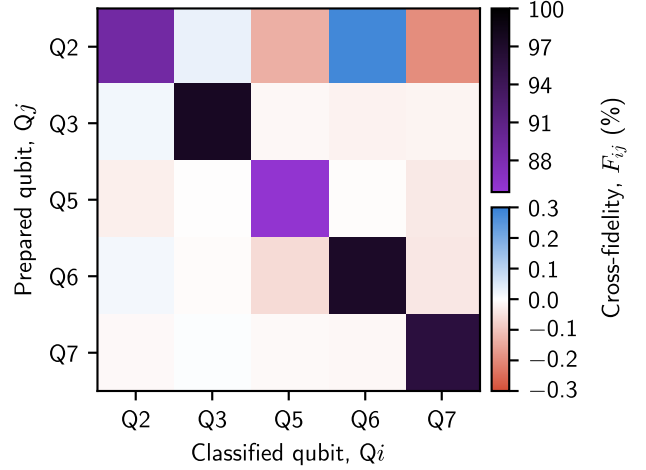

FIG. 9. Cross-fidelity calculated using Eq. (E1). The diagonal elements correspond to the single qubit readout fidelities.

to qubit i may carry additional information about qubit j without causing imperfections visible in cross-fidelity F_{ij}. The complete physical influence on qubit j from a readout pulse at qubit i is characterized by the parasitic measurement-induced dephasing discussed in the Section V.

Another method to look for crosstalk in the data is to consider the cross-correlation matrix averaged over all prepared states

$$C_{ij} = \left\langle \frac{\text{cov}\,(\sigma_{zi}, \sigma_{zj})}{\sqrt{\text{var}\,(\sigma_{zi})\,\text{var}\,(\sigma_{zj})}}\right\rangle, \tag{E2}$$

shown in Fig. 10. The positive (negative) cross-correlation indicates an over-representation of qubit pairs assigned to the same (opposite) state. As all states are prepared with an equal weight, we expect no cross-correlations while the diagonal elements $C_{ii} = 1$ by definition. The off-diagonal elements of Fig 10 are close to zero, thus we again see evidence that errors from correlations in the readout are significantly smaller than single-qubit errors. While correlation matrix indeed quantifies the crosstalk in the assignment, it has some drawbacks. For example in the trivial situation where the readout pulse would be turned off, the qubit state assignment would be highly correlated. Similarly, if the assignment of qubit i to the exited state would always cause a bit-flip in the assignment of qubit j, the correlation-matrix element C_{ij} would still be zero, as C_{ij} is averaged over all qubit preparations. Thus the correlation matrix has limited applications for characterizing on-chip readout crosstalk.

Appendix F: Measurement efficiency

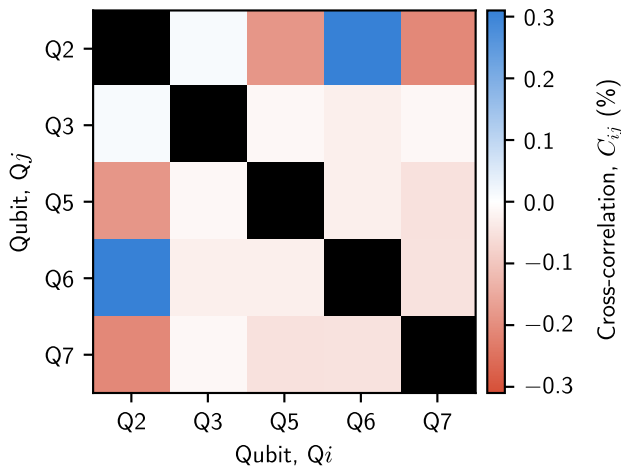The measurement-induced dephasing and the single-shot histograms give information about the measurement

FIG. 10. Correlation coefficients between the outcomes of the multiplexed single-shot measurements as calculted by Eq. (E2)

efficiency [44]. The measurement-induced dephasing can be obtained from a Ramsey experiment with a measurement pulse interleaved between the two $\pi/2$-pulses also discussed in Section V. The average dephasing rates for each qubit are the diagonal elements, Γ_{ii}, of Fig. 7, which are extracted by fitting a Gaussian to the Ramsey signal as a function of varying measurement pulse amplitude [44]. In addition, from the single-shot histograms, such as the ones shown in Fig. 5, we can extract the signal to noise ration (SNR), as the difference between the mean of the ground and excited state distributions divided by the

standard deviation σ:

$$\mathrm{SNR} = \frac{\langle s \rangle_\pi - \langle s \rangle_0}{\sigma}, \tag{F1}$$

where $\langle s \rangle_{\pi(0)}$ is the average measured signal, s, when preparing the qubit with (without) a π-pulse prior to readout pulse and σ is the standard deviation of the signal.

	Q2	Q3	Q5	Q6	Q7
Efficiency, η	51.8%	49.9%	42.7%	51.2%	47.9%

TABLE IV. The measurement efficiency for each qubit calculated by Eq. (F2) from a Ramsey type measurement discussed in the main text.

As shown in Ref. [44], the quantum limited SNR can be expressed in terms of the integrated measurement induced dephasing, $\Gamma_{ii}\tau_p$, such that

$$\eta_i = \frac{\mathrm{SNR}^2}{4\Gamma_{ii}\tau_p}. \tag{F2}$$

The observed measurement efficiencies are in the range of 42% to 52% as listed in Table IV. The measurement efficiency is limited by the internal loss in the TWPA [26] and in the MW components between the sample and TWPA. The differences of the measurement efficiency between each qubit may be explained by a frequency dependency in the gain of the TWPA and in the rest of the detection chain.

[1] M. A. Nielsen and I. L. Chuang, Phys. Rev. Lett. **79**, 321 (1997).
[2] D. P. DiVincenzo, Phys. Scr. **2009**, 014020 (2009).
[3] R. Barends, J. Kelly, A. Megrant, A. Veitia, D. Sank, E. Jeffrey, T. C. White, J. Mutus, A. G. Fowler, B. Campbell, Y. Chen, Z. Chen, B. Chiaro, A. Dunsworth, C. Neill, P. OMalley, P. Roushan, A. Vainsencher, J. Wenner, A. N. Korotkov, A. N. Cleland, and J. M. Martinis, Nature **508**, 500 (2014).
[4] C. H. Bennett, G. Brassard, C. Crépeau, R. Jozsa, A. Peres, and W. K. Wootters, Phys. Rev. Lett. **70**, 1895 (1993).
[5] L. Steffen, Y. Salathe, M. Oppliger, P. Kurpiers, M. Baur, C. Lang, C. Eichler, G. Puebla-Hellmann, A. Fedorov, and A. Wallraff, Nature **500**, 319 (2013).
[6] J. E. Johnson, C. Macklin, D. H. Slichter, R. Vijay, E. B. Weingarten, J. Clarke, and I. Siddiqi, Phys. Rev. Lett. **109**, 050506 (2012).
[7] D. Ristè, J. G. van Leeuwen, H.-S. Ku, K. W. Lehnert, and L. DiCarlo, Phys. Rev. Lett. **109**, 050507 (2012).
[8] Y. Salathé, P. Kurpiers, T. Karg, C. Lang, C. K. Andersen, A. Akin, C. Eichler, and A. Wallraff, arXiv:1709.01030 (2017).

[9] M. Jerger, S. Poletto, P. Macha, U. Hbner, E. Ilichev, and A. V. Ustinov, Applied Physics Letters **101**, 042604 (2012), http://dx.doi.org/10.1063/1.4739454.
[10] V. Schmitt, X. Zhou, K. Juliusson, B. Royer, A. Blais, P. Bertet, D. Vion, and D. Esteve, Phys. Rev. A **90**, 062333 (2014).
[11] E. Jeffrey, D. Sank, J. Y. Mutus, T. C. White, J. Kelly, R. Barends, Y. Chen, Z. Chen, B. Chiaro, A. Dunsworth, A. Megrant, P. J. J. O'Malley, C. Neill, P. Roushan, A. Vainsencher, J. Wenner, A. N. Cleland, and J. M. Martinis, Phys. Rev. Lett. **112**, 190504 (2014).
[12] A. Blais, R.-S. Huang, A. Wallraff, S. M. Girvin, and R. J. Schoelkopf, Phys. Rev. A **69**, 062320 (2004).
[13] A. Wallraff, D. I. Schuster, A. Blais, L. Frunzio, J. Majer, M. H. Devoret, S. M. Girvin, and R. J. Schoelkopf, Phys. Rev. Lett. **95**, 060501 (2005).
[14] C. M. Caves, Phys. Rev. D **26**, 1817 (1982).
[15] B. Yurke, M. L. Roukes, R. Movshovich, and A. N. Pargellis, Appl. Phys. Lett. **69**, 3078 (1996).
[16] M. A. Castellanos-Beltran, K. D. Irwin, G. C. Hilton, L. R. Vale, and K. W. Lehnert, Nat. Phys. **4**, 929 (2008).
[17] C. Eichler, Y. Salathe, J. Mlynek, S. Schmidt, and A. Wallraff, Phys. Rev. Lett. **113**, 110502 (2014).

[18] F. Mallet, F. R. Ong, A. Palacios-Laloy, F. Nguyen, P. Bertet, D. Vion, and D. Esteve, Nat. Phys. **5**, 791 (2009).

[19] R. Vijay, D. H. Slichter, and I. Siddiqi, Phys. Rev. Lett. **106**, 110502 (2011).

[20] M. D. Reed, B. R. Johnson, A. A. Houck, L. DiCarlo, J. M. Chow, D. I. Schuster, L. Frunzio, and R. J. Schoelkopf, Appl. Phys. Lett. **96**, 203110 (2010).

[21] N. T. Bronn, Y. Liu, J. B. Hertzberg, A. D. Córcoles, A. A. Houck, J. M. Gambetta, and J. M. Chow, Applied Physics Letters **107**, 172601 (2015).

[22] T. Walter, P. Kurpiers, S. Gasparinetti, P. Magnard, A. Potocnik, Y. Salathé, M. Pechal, M. Mondal, M. Oppliger, C. Eichler, and A. Wallraff, Phys. Rev. Applied **7**, 054020 (2017).

[23] S. Filipp, P. Maurer, P. J. Leek, M. Baur, R. Bianchetti, J. M. Fink, M. Göppl, L. Steffen, J. M. Gambetta, A. Blais, and A. Wallraff, Phys. Rev. Lett. **102**, 200402 (2009).

[24] L. DiCarlo, M. D. Reed, L. Sun, B. R. Johnson, J. M. Chow, J. M. Gambetta, L. Frunzio, S. M. Girvin, M. H. Devoret, and R. J. Schoelkopf, Nature **467**, 574 (2010).

[25] J. Y. Mutus, T. C. White, R. Barends, Y. Chen, Z. Chen, B. Chiaro, A. Dunsworth, E. Jeffrey, J. Kelly, A. Megrant, C. Neill, P. J. J. O'Malley, P. Roushan, D. Sank, A. Vainsencher, J. Wenner, K. M. Sundqvist, A. N. Cleland, and J. M. Martinis, Applied Physics Letters **104**, 263513 (2014).

[26] C. Macklin, K. O'Brien, D. Hover, M. E. Schwartz, V. Bolkhovsky, X. Zhang, W. D. Oliver, and I. Siddiqi, Science **350**, 307 (2015).

[27] T. Roy, S. Kundu, M. Chand, A. M. Vadiraj, A. Ranadive, N. Nehra, M. P. Patankar, J. Aumentado, A. A. Clerk, and R. Vijay, Appl. Phys. Lett. **107**, 262601 (2015).

[28] C. Neill, P. Roushan, K. Kechedzhi, S. Boixo, S. V. Isakov, V. Smelyanskiy, R. Barends, B. Burkett, Y. Chen, Z. Chen, B. Chiaro, A. Dunsworth, A. Fowler, B. Foxen, R. Graff, E. Jeffrey, J. Kelly, E. Lucero, A. Megrant, J. Mutus, M. Neeley, C. Quintana, D. Sank, A. Vainsencher, J. Wenner, T. C. White, H. Neven, and J. M. Martinis, arXiv:1709.06678 (2017).

[29] N. T. Bronn, B. Abdo, K. Inoue, S. Lekuch, A. D. Crcoles, J. B. Hertzberg, M. Takita, L. S. Bishop, J. M. Gambetta, and J. M. Chow, Journal of Physics: Conference Series **834**, 012003 (2017).

[30] A. Corcoles, E. Magesan, S. J. Srinivasan, A. W. Cross, M. Steffen, J. M. Gambetta, and J. M. Chow, Nat Commun **6**, (2015).

[31] M. Reagor, C. B. Osborn, N. Tezak, A. Staley, G. Prawiroatmodjo, M. Scheer, N. Alidoust, E. A. Sete, N. Didier, M. P. da Silva, E. Acala, J. Angeles, A. Bestwick, M. Block, B. Bloom, A. Bradley, C. Bui, S. Caldwell, L. Capelluto, R. Chilcott, J. Cordova, G. Crossman, M. Curtis, S. Deshpande, T. E. Bouayadi, D. Girshovich, S. Hong, A. Hudson, P. Karalekas, K. Kuang, M. Lenihan, R. Manenti, T. Manning, J. Marshall, Y. Mohan, W. OB́rien, J. Otterbach, A. Papageorge, J. Paquette, M. Pelstring, A. Polloreno, V. Rawat, C. A. Ryan, R. Renzas, N. Rubin, D. Russell, M. Rust, D. Scarabelli, M. Selvanayagam, R. Sinclair, R. Smith, M. Suska, T. . To, M. Vahidpour, N. Vodrahalli, T. Whyland, K. Yadav, W. Zeng, and C. T. Rigetti, arXiv:1706.06570 (2017).

[32] C. C. Bultink, M. A. Rol, T. E. O'Brien, X. Fu, B. C. S. Dikken, C. Dickel, R. F. L. Vermeulen, J. C. de Sterke, A. Bruno, R. N. Schouten, and L. DiCarlo, Phys. Rev. Applied **6**, 034008 (2016).

[33] S. Asaad, C. Dickel, N. K. Langford, S. Poletto, A. Bruno, M. A. Rol, D. Deurloo, and L. DiCarlo, Npj Quantum Information **2**, 16029 (2016).

[34] C. Song, K. Xu, W. Liu, C.-p. Yang, S.-B. Zheng, H. Deng, Q. Xie, K. Huang, Q. Guo, L. Zhang, P. Zhang, D. Xu, D. Zheng, X. Zhu, H. Wang, Y.-A. Chen, C.-Y. Lu, S. Han, and J.-W. Pan, Phys. Rev. Lett. **119**, 180511 (2017).

[35] A. G. Fowler, M. Mariantoni, J. M. Martinis, and A. N. Cleland, Phys. Rev. A **86**, 032324 (2012).

[36] R. B. Griffiths and C.-S. Niu, Phys. Rev. Lett. **76**, 3228 (1996).

[37] C. H. Bennett, G. Brassard, S. Popescu, B. Schumacher, J. A. Smolin, and W. K. Wootters, Phys. Rev. Lett. **76**, 722 (1996).

[38] B. Yurke and D. Stoler, Phys. Rev. A **46**, 2229 (1992).

[39] E. A. Sete, J. M. Martinis, and A. N. Korotkov, Phys. Rev. A **92**, 012325 (2015).

[40] J. Gambetta, A. Blais, D. I. Schuster, A. Wallraff, L. Frunzio, J. Majer, M. H. Devoret, S. M. Girvin, and R. J. Schoelkopf, Phys. Rev. A **74**, 042318 (2006).

[41] J. Koch, T. M. Yu, J. Gambetta, A. A. Houck, D. I. Schuster, J. Majer, A. Blais, M. H. Devoret, S. M. Girvin, and R. J. Schoelkopf, Phys. Rev. A **76**, 042319 (2007).

[42] R. Barends, J. Kelly, A. Megrant, D. Sank, E. Jeffrey, Y. Chen, Y. Yin, B. Chiaro, J. Mutus, C. Neill, P. O'Malley, P. Roushan, J. Wenner, T. C. White, A. N. Cleland, and J. M. Martinis, Phys. Rev. Lett. **111**, 080502 (2013).

[43] J. Gambetta, W. A. Braff, A. Wallraff, S. M. Girvin, and R. J. Schoelkopf, Phys. Rev. A **76**, 012325 (2007).

[44] C. C. Bultink, B. Tarasinski, N. Haandbaek, S. Poletto, N. Haider, D. J. Michalak, A. Bruno, and L. DiCarlo, arXiv:1711.05336 (2017).

[45] X. Y. Jin, A. Kamal, A. P. Sears, T. Gudmundsen, D. Hover, J. Miloshi, R. Slattery, F. Yan, J. Yoder, T. P. Orlando, S. Gustavsson, and W. D. Oliver, Phys. Rev. Lett. **114**, 240501 (2015).

[46] M. Boissonneault, J. M. Gambetta, and A. Blais, Phys. Rev. A **79**, 013819 (2009).

[47] D. H. Slichter, R. Vijay, S. J. Weber, S. Boutin, M. Boissonneault, J. M. Gambetta, A. Blais, and I. Siddiqi, Phys. Rev. Lett. **109**, 153601 (2012).

[48] R. Versluis, S. Poletto, N. Khammassi, B. Tarasinski, N. Haider, D. J. Michalak, A. Bruno, K. Bertels, and L. DiCarlo, Phys. Rev. Applied **8**, 034021 (2017).

[49] C. W. Gardiner and M. J. Collett, Phys. Rev. A **31**, 3761 (1985).

[50] J. Bourassa, F. Beaudoin, J. M. Gambetta, and A. Blais, Phys. Rev. A **86**, 013814 (2012).